MICROROBOTS

In situ integrated microrobots driven by artificial muscles built from biomolecular motors

Yingzhe Wang[1]*, **Takahiro Nitta**[2], **Yuichi Hiratsuka**[3], **Keisuke Morishima**[1,4]*

Microrobots have been developed for applications in the submillimeter domain such as the manipulation of micro-objects and microsurgery. Rapid progress has been achieved in developing miniaturized components for microrobotic systems, resulting in a variety of functional microactuators and soft components for creating untethered microrobots. Nevertheless, the integration of microcomponents, especially the assembly of actuators and mechanical components, is still time-consuming and has inherent restrictions, thus limiting efficient fabrications of microrobots and their potential applications. Here, we propose a method for fabricating microrobots in situ inspired by the construction of microsystems in living organisms. In a microfluidic chip, hydrogel mechanical components and artificial muscle actuators are successively photopatterned from hydrogel prepolymer and biomolecular motors, respectively, and integrated in situ into functional microrobots. The proposed method allows the fast fabrication of microrobots through simple operations and affordable materials while providing versatile functions through the precise spatiotemporal control of in situ integration and reconfiguration of artificial muscles. To validate the method, we fabricated microrobots to elicit different motions and on-chip robots with unique characteristics for microfluidic applications. This study may establish a new paradigm for microrobot integration and lead to the production of unique biohybrid microrobots with various advantages.

INTRODUCTION

In the past few decades, intelligent microrobots have been increasingly investigated (*1*–*4*). By miniaturizing components and systems, microrobots are expected to perform sophisticated tasks at small scales, such as cell localization, targeted drug delivery, and minimally invasive surgery (*5*). Recently, microrobot development has been transitioning from hard and rigid structures to soft and flexible architectures (*6*). Inspired by biological systems in nature, which can dynamically change their shape, structure, and function to adapt to the environment, researchers have focused on developing miniaturized soft components to create untethered soft microrobots (*7*, *8*).

The fabrication of untethered soft microrobots has revealed the limitations of conventional assembly and integration methods. Typically, microcomponents including actuators and mechanical structures are prepared in different places through different micromachining processes and then assembled into a functional microrobot (fig. S1A). Although rapid progress has been made in improving micromachining techniques (*9*–*12*) and developing new materials for microactuators, including soft active materials (*13*–*15*) and living biomaterials (*3*, *16*–*18*), the assembly and integration of microcomponents remain challenging. Serial pick-and-place robotic assembly is generally used to build microrobots (*19*). However, for microcomponents, conventional assembly is extremely slow and costly owing to the complicated control required to manipulate objects with high accuracy (*20*). For flexible objects, the estimation of the deformation and the avoidance of damage further increase the difficulty in their control. Moreover, strong parasitic stiction forces between a robotic tweezer and microcomponents hinder pick-and-place assembly at the microscopic level, especially for soft materials (*21*). Other assembly methods—such as multilayer soft lithography (*9*), metallization (*22*), and self-assembly of living tissues (*23*, *24*)—also present major limitations regarding efficiency, cost, and flexibility.

Nature may provide inspiration to circumvent the limitations of conventional assembly methods. Unlike multiple-site assembly, biological systems such as cells, tissues, and organs are self-assembled from the bottom up through coordinated supramolecular and cellular processes (*25*). For example, during the development of the limb musculoskeletal system of mice, the limb primary skeleton structure and muscle are first developed through the differentiation and proliferation of mesenchymal cells and myogenic cells; then, bone eminences and tendons are formed between the skeleton and muscle, connecting them to form a functional limb (*26*). If microrobots can be in situ constructed in a similar way (fig. S1B), untethered systems may be easier to obtain while avoiding complex assembly and integration, thereby reducing costs related to production time, labor, and equipment.

In situ fabrication has been demonstrated for the creation of entirely soft robots (*27*, *28*). Key to its success for application in microrobots is a suitable active material, which can be patterned into desired two-dimensional (2D) or 3D structures through micromachining and can autonomously assemble with the target mechanical structure after patterning. In this context, we considered biomolecular motors, the protein machines in living cells that convert chemical energy into mechanical work efficiently (*29*). Recent studies have demonstrated that the protein machines can consist of active contractile materials in vitro (*30*–*33*). Some progress has been made in artificially organizing molecular motors into large arrays that can achieve the level of force and movement generation achieved by these contractile filaments in living cells (*34*, *35*). In previous work, we introduced a photo-induced contractile network of molecular motors (fig. S2) (*36*). Under ultraviolet (UV) irradiation, a muscle-like

---

[1]Department of Mechanical Engineering, Osaka University, 2-1 Yamada-oka, Suita, Osaka 565-0871, Japan. [2]Applied Physics Course, Faculty of Engineering, Gifu University, 1-1 Yanagido, Gifu City 501-1193, Japan. [3]School of Materials Science, Japan Advanced Institute of Science and Technology (JAIST), 1-1 Asahidai, Nomi, Ishikawa 923-1292, Japan. [4]Center for Medical Engineering and Informatics, Osaka University, 2-1 Yamada-oka, Suita, Osaka 565-0871, Japan.
*Corresponding author. Email: ywang@live.mech.eng.osaka-u.ac.jp (Y.W.); morishima@mech.eng.osaka-u.ac.jp (K.M.)

hierarchical organization consisting of microtubules, a fusion protein of calmodulin and light meromyosin (CaMLMM), and another fusion protein of kinesin-1 and calmodulin-binding sequence m13 (K465m13) is formed. It can anchor the pillars in the irradiated area, generating a micronewton tension force. This artificial muscle amplifies the nanometer-scale action of molecular motors to macroscopic movements of engineering systems. Owing to its scalable printability and considerable contractility, it holds promise for microrobot applications (*37*).

Here, we propose a method for in situ fabrication of microrobots (Fig. 1). In a microfluidic chip, a hydrogel mechanical structure and artificial muscle actuators were successively patterned through optofluidic lithography (*38*–*41*) and integrated in situ into a functional robotic system. Poly(ethylene glycol) diacrylate (PEGDA) hydrogel has been used owing to its tunable mechanical properties, its excellent biocompatibility and stability (*42*, *43*), and its ability to move in aqueous environments with the aid of non-ionic surfactants (*44*, *45*). We characterized the mechanical properties of PEGDA hydrogel and the contractility of the artificial muscle to improve microrobot design. In situ microfluidic integration of hydrogel mechanical structures and artificial muscle actuators increases fabrication efficiency and can be precisely controlled both spatially and temporally. These characteristics allow for the fast fabrication of microrobots with complex spatial architectures and time-dependent functions as well as the reconfiguration of actuators to achieve repeatable actuation or function switching. To validate the proposed method, we report the fabrication and operation of microrobots with different functions, including a gripper, a fish, a walker, and a robot arm. In addition, the fabrication and operation of a three-way valve and a gated cage for microfluidic applications are presented.

RESULTS

In situ microrobot fabrication

Figure 1 illustrates the proposed fabrication method of microrobots in a microfluidic chip to produce a microrobot with gripping motion,

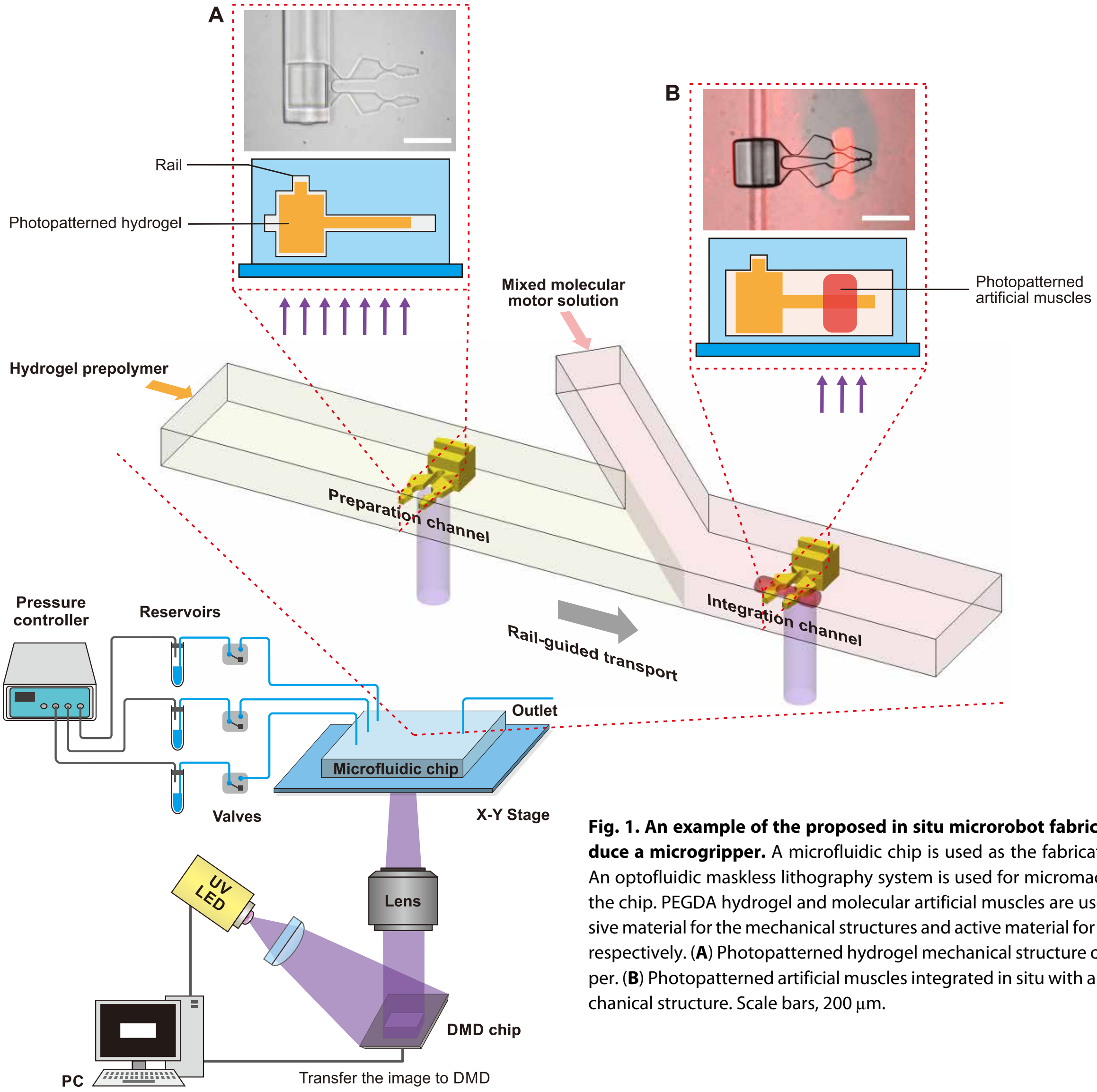

Fig. 1. An example of the proposed in situ microrobot fabrication to produce a microgripper. A microfluidic chip is used as the fabrication platform. An optofluidic maskless lithography system is used for micromachining inside the chip. PEGDA hydrogel and molecular artificial muscles are used as the passive material for the mechanical structures and active material for the actuators, respectively. (**A**) Photopatterned hydrogel mechanical structure of a microgripper. (**B**) Photopatterned artificial muscles integrated in situ with a hydrogel mechanical structure. Scale bars, 200 μm.

which is notable in handling objects, especially fragile items. The chip was made of polydimethylsiloxane (PDMS) and contained several microchannels for mixing, preparation, and integration. An experimental setup was constructed to enable precise flow control and digital maskless lithography inside the microchannels.

First, the mechanical structures of microrobots were prepared. A hydrogel prepolymer solution was introduced into the preparation channel and patterned with UV irradiation. A finned hydrogel microstructure was polymerized with cantilever beams or pillars as anchors for the artificial muscle. The microscopic image in Fig. 1 shows the polymerized mechanical structure of the microgripper. During photopolymerization, an un–cross-linked lubricating layer was formed between the hydrogel and PDMS channel for the polymerized hydrogel to free-float in the channel (*46*, *47*). The fin fitting in the microchannel rail allowed the transport of the polymerized hydrogel along the rail via transporting flow (*40*, *48*). Complex mechanical structures could be built through the rail-guided assembly of hydrogel components. After polymerization and assembly, the mechanical structure was transported to an actuation channel and fixed by a slot in the rail. Then, 0.5% Triton X-100 solution was introduced into the channel to remove the residual prepolymer, and the hydrogel structure was swollen by water absorption (*49*).

In this process, PEGDA hydrogel with different concentrations (20 to 80%) was available and was polymerized with suitable induction conditions. The final geometry of hydrogel microstructures was precisely controlled according to the characterized thickness of the oxygen inhibition layer (fig. S8) and the swelling ratio in aqueous solution (fig. S9). Optionally, intricate 3D microstructures could be patterned through multistep polymerization, in which the structure was polymerized part by part using different materials in microchannels with different heights (Fig. 2A). Furthermore, fabrication with two types of hydrogels was applied to construct movable mechanical joints (Fig. 2B). Specifically, hydrophilic PEGDA hydrogel and hydrophobic poly(propylene glycol) diacrylate (PPGDA) hydrogel were used to pattern the adjacent links of a joint to avoid self-adhesion between the hydrogel structures (*50*, *51*).

Second, the artificial muscle actuators were integrated in situ (Fig. 1). Solution A, containing CaMLMM and K465m13, and solution B, containing microtubules and *o*-nitrophenyl EGTA, were equally mixed in a mixing channel and then introduced into the actuation channel. This split injection was to avoid the decrease in the concentration of adenosine triphosphate (the energy source of the artificial muscles) caused by the reaction of K465m13 with microtubules in the premixed solution. Using image-based shape detection, patterned UV irradiation was aligned with the prepared mechanical structure and activated the molecular motors in this area. Contracting artificial muscles were soon formed, wrapping the anchors and performing the assigned functions. The merged bright-field/fluorescent image in Fig. 1 shows the microgripper closed by the integrated artificial muscles 12 s after UV irradiation.

In this process, the initial conformation of formed artificial muscle depended on the space that molecular motors were photoinduced, that is, the intersection of the lithography light beam and the microchannel, and the direction of contraction and generated force depended on the relative positions of the anchors in this space. A typical strategy was to induce the molecular motors in a cuboid space surrounding two parallel anchors, thus effectively transmitting the force and linear displacement of the artificial muscle to the anchors (Fig. 2C). An appropriate diameter of the anchors, *d*, was required, typically from 20 to 300 μm. Sufficient D_p, the distance

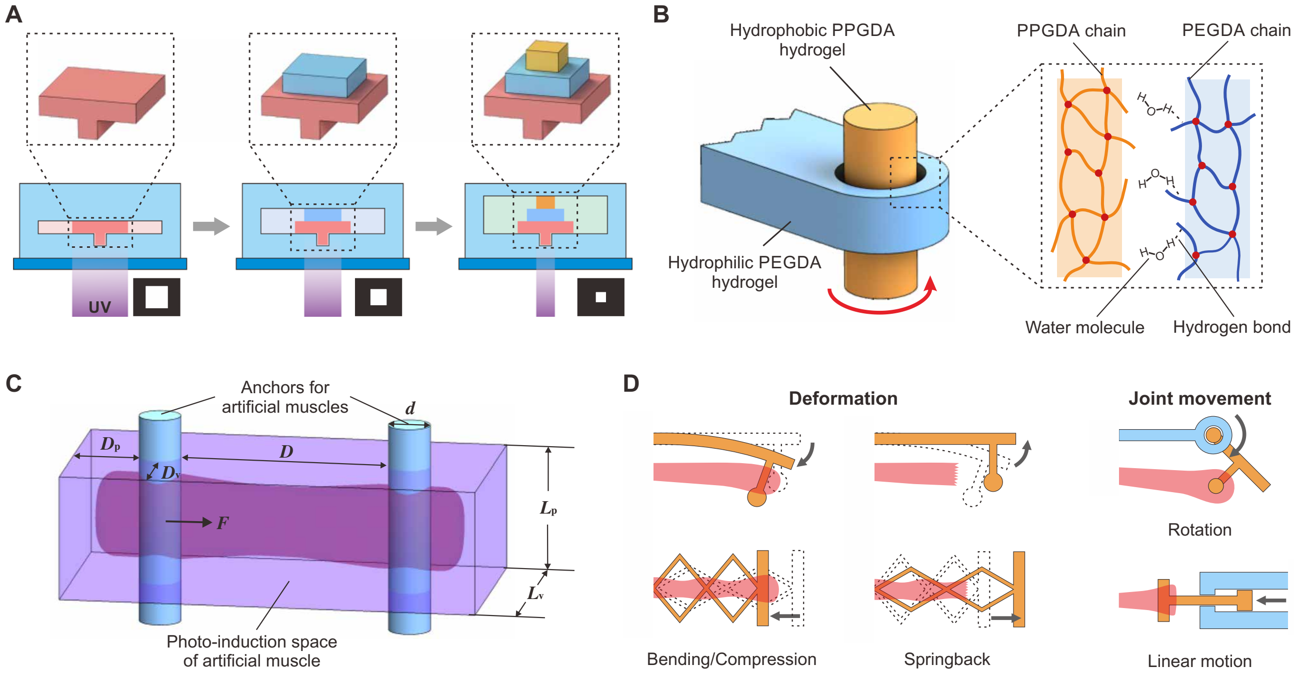

Fig. 2. Fabrication strategy for the microrobots. (**A**) Schematic diagram of the multistep polymerization strategy for achieving complex 3D microstructures. (**B**) Schematic diagram of the multihydrogel fabrication strategy for achieving movable mechanical joints. Self-adhesion between the two links caused by hydrogen bonds can be avoided. (**C**) Schematic diagram of the typical photopatterning of artificial muscle and related parameters. (**D**) Possible designs for microrobots created by the in situ fabrication process.

between the anchors and the edge of the induction space in the direction parallel to the contraction, and D_v, the distance in the direction perpendicular to the contraction, ensured tight anchoring during contraction, typically more than twice d. Conversely, by adjusting D_p and D_v, the artificial muscle could be controlled to break away from the anchor at the desired timing. The maximum possible force acting on the anchors mainly depended on the cross-sectional area of the induction space (values of L_p, the length in the direction parallel to the anchors, and L_v, the length in the direction perpendicular to the anchors), with an increase of L_p being more effective for improving the contractility than an increase of L_v. By combining multiple such basic units, multidirectional contraction could be achieved, which permitted the programming of microrobots for more sophisticated applications.

The microgripper was fabricated within 3 min (movie S1), requiring far less time and no complex operation as compared with ones integrated by conventional means, such as robotic assembly (*52*), multilayer lithography (*53*), and cell culture (*54*), which made it suitable for applications that require on-site fabrication on-demand. In addition, in the repetition of the fabrication process (movie S1), the geometry of patterned mechanical structures and the artificial muscles, the consumed time, and the movement of integrated microgrippers remained consistent. This demonstrated the reproducibility of our fabrication method. Moreover, scalable fabrication was achieved in which multiple mechanical structures were prepared and artificial muscles were subsequently integrated (movie S2).

Actuator reconfiguration

Besides the in situ fabrication process, we leveraged the facile flow control of microfluidics to reconfigure artificial muscle actuators in microrobots for repeated actuation or function switching. Immediately after an actuation process was completed, a new molecular motor solution was replenished into the channel. The contracted motor network was torn apart and detached from the microrobot with the flow. Alternatively, a 1% sodium dodecyl sulfate solution was introduced to fully remove contracted artificial muscles before the replenishment of the molecular motor solution. Then, new artificial muscles could be patterned in the same position to repeat the actuation or in other positions to perform other functions.

As a proof of concept, we fabricated a fish-like microrobot that can perform cyclical swinging, mimicking the natural motion of a fish (Fig. 3). The microfish had a length of 1250 μm and a thickness of 40 μm. After polymerization, it was transported to an actuation channel with a thickness of 250 μm and fixed there. The artificial muscles were first photopatterned, wrapping the spines on one side of the body and bending it to an angle of around 25°. The force acting on the spines was calculated to be about 0.5 μN. After contraction, the artificial muscles were reconfigured on the other side, and the bending direction was switched. This process was alternated through quick replenishment of the molecular motor solution, and the microfish swung cyclically (Fig. 3B and movie S3). More than four swing cycles were achieved with a 5-μl solution, and the interval between each cycle was approximately 300 s. We measured the maximum swing angle α per actuation for evaluation (Fig. 3C). Despite the influence of the residual artificial muscle, the maximum swing angle did not decrease substantially with the increase in actuation time. The cyclical swinging test was repeated three times using independently fabricated microfishes. The mean maximum angles in each test were 25 ± 3°, 25 ± 6°, and 24 ± 3°, and no significant difference was noted ($P = 0.613$), which further indicated the reproducibility of the fabrication method. This repeated bending motion is potentially useful for the study of flapping-induced fluid dynamics and fatigue testing of biological microstructures.

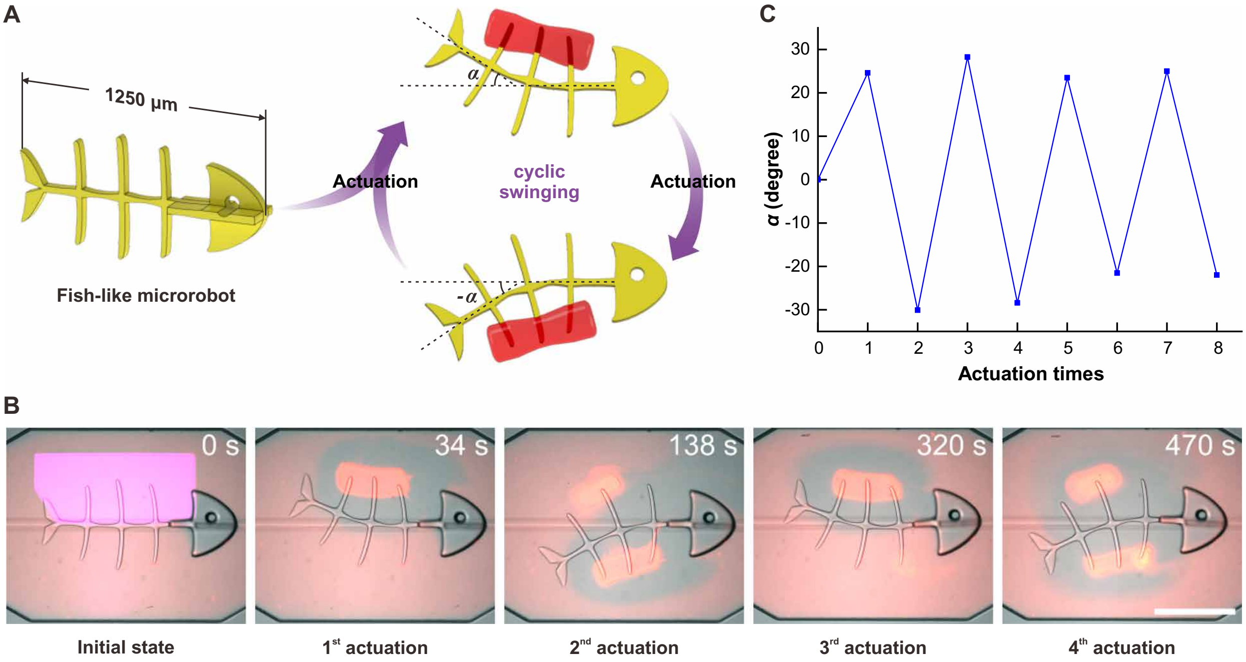

Fig. 3. Fish-like microrobot demonstrating reconfiguration. (**A**) Schematic diagram of the fish-like robot and its cyclic swinging by continuous reconfiguration of artificial muscles. (**B**) Actuation sequence of the fish-like robot (movie S3). (**C**) Swing angle per actuation process. No considerable decrease in swing angle was observed with more actuation. Scale bar, 500 μm.

Spatiotemporal control of integration

In addition to increasing efficiency and providing reconfigurability, in situ integration can be controlled with high spatiotemporal precision. The artificial muscles can be patterned in the desired 3D shapes and at desired locations to be precisely assembled with the mechanical structures. This enables the selective integration of actuators and the complex integration of actuators with mechanical structures, enabling strategies such as nested assemblies, which are difficult to achieve using conventional fabrication methods. Furthermore, artificial muscles can be patterned and assembled with mechanical structures considering specific timings and sequences, allowing microrobots to perform time-dependent tasks.

To demonstrate spatiotemporal control, we fabricated a microrobot endowed with a walking function, a common way toward mobile microrobots (*55*). The microrobot consisted of a pantograph-shaped body with four legs, and two slits were designed at each end of the body as anchors for the artificial muscle (Fig. 4A). The motion of this microwalker was based on the friction difference between contracting and breaking [fig. S3 (*56*)]. We simulated the deformation of the mechanical structure caused by the contraction of the artificial muscles using the COMSOL Multiphysics software (Fig. 4B). For a force of 1.2 μN exerted on the slits and by fixing the backplane of the body, the distance between the front and rear legs was reduced by about 120 μm, which was sufficient to cause forward movement. The hydrogel mechanical structure was rapidly prepared through three-step polymerization (Fig. 4, C and D). The sequences in Fig. 4E and movie S4 show the integration of the artificial muscle. According to the tilting of the mechanical structure, the artificial muscles were photopatterned at the corresponding angle and accurately wrapped around the body at the slits. The microwalker displayed forward walking with the contraction of the artificial muscles, although the front and rear legs slipped during both contracting and breaking. Figure 4F shows the displacement of the front and rear leg tips. In 78 s, the microwalker moved approximately 72 μm, reaching an average velocity of 0.92 μm/s. Three microwalkers were fabricated independently, and similar performances were observed, as shown in Table 1. The average reduced distance between the front and rear leg tips was 248 ± 24.8 μm, which was larger than

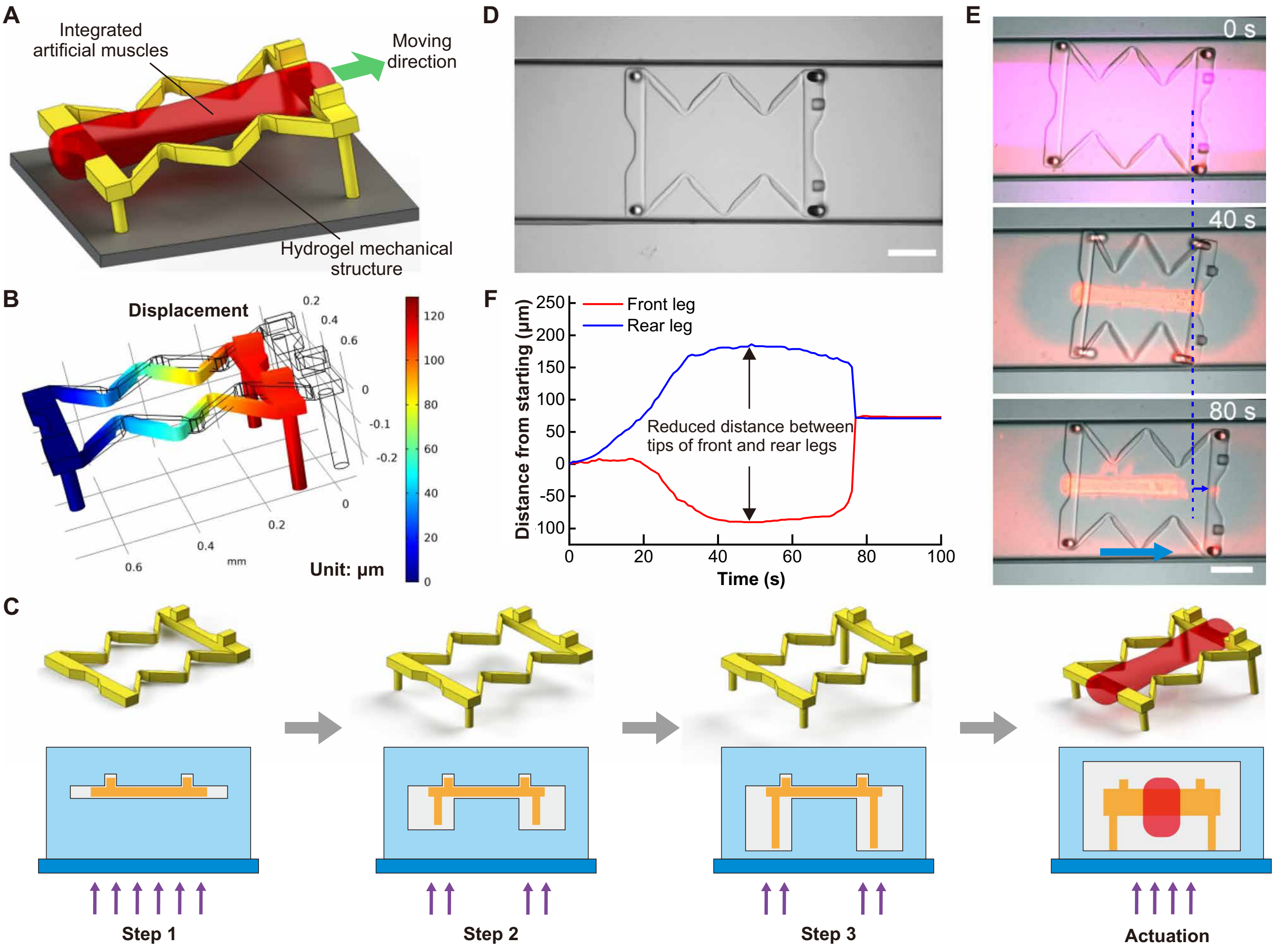

Fig. 4. Microwalker demonstrating spatiotemporal controllability of in situ integration. (**A**) Schematic diagram of the microwalker. (**B**) Deformation simulation results of the microwalker. The maximum displacement of 120 μm was obtained at the top of the front legs. (**C**) Three-step polymerization procedure of the hydrogel mechanical structure. (**D**) Prepared hydrogel mechanism of the microwalker in the actuation channel. (**E**) Walking sequence of the microwalker driven by precisely integrated artificial muscles (movie S4). (**F**) Positions of front and rear leg tips over time. The positive direction of the *y* axis was set to the designed moving direction from the starting position. The starting position was set as the origin. Scale bars, 200 μm.

Table 1. Performance values of microwalkers.

	Reduced distance (μm)	Moving distance (μm)	Consumed time (s)	Average velocity (μm/s)
First	271.8	72.0	78	0.92
Second	224.3	68.5	65	1.05
Third	250.6	65.3	74	0.88

the simulation prediction. This difference may be attributable to oxygen inhibition during polymerization, which narrows the joints of the hydrogel body compared with their designed width. Moreover, the additional space below the hydrogel body causes the self-assembly of more molecular motors in that space, and the resulting tensile force acting on the body inclines it downward relative to its axis, making the body arch upward. With further improvement of the artificial muscle, faster and long-lasting walking is expected, giving this bio-driven, biocompatible, and biodegradable microwalker promising potential in medical interventions such as targeted drug delivery.

We also fabricated a microrobot arm connecting a PEGDA upper arm and a PPGDA forearm by a pinned rotary joint (Fig. 5A). The joint rotated when integrating the artificial muscles on one side of the arm. This mechanism mimics the musculoskeletal system in the human body and uses tendon-like pillars for efficient force transmission (*57*). The microrobot arm was quickly prepared using multihydrogel fabrication (Fig. 5B and movie S5). An actuation test was conducted by bidirectionally rotating the robot arm joint when artificial muscles were sequentially photopatterned on the left and right sides (Fig. 5C and movie S6), which was estimated to generate a force of 0.8 μN on the pillar of the forearm and a torque of 9.6×10^{-11} N·m on the joint at maximum, according to the contractile characterization (fig. S11). Because the resistance torque on the joint was relatively small, the rotation angle depended on the maximum displacement of the artificial muscle. Figure 5D shows the joint rotation angles, whose peaks were approximately 74° and −57° at 35 and 64 s after UV irradiation, respectively. The same test was conducted using a microrobot arm made of only PEGDA hydrogel (movie S7), whose sluggish rotation indicated a large resistance force at the joint. This comparison illustrates the effectiveness of multihydrogel fabrication to create freely movable mechanical joints.

We then fabricated two microrobot arms and actuated them to grab a microball through sequential finger-like motions (Fig. 5E and movie S8). First, the right arm was actuated to push the ball to the middle position. Then, the left arm was actuated such that the two forearms were folded together, trapping the ball in the enclosure. This experiment illustrates the scalability of our fabrication method and the potential of microrobot arms to elicit various manipulation behaviors.

Microfluidic applications

The proposed method allows for the in situ fabrication of microrobots with versatile functions for several applications. An application is the fabrication of on-chip robots in microfluidics for efficient regulation of fluids at the microscopic scale or dexterous manipulation of micro-objects, which are critical to lab-on-a-chip systems (*58*, *59*).

We evaluated two examples of microfluidic application. The first example was a three-way valve made of a hydrogel core installed in a Y-shaped channel with one of its ends confined in a circular slot (Fig. 6A). There was a pillar on each side of the valve core, and each outlet had a fixed PDMS pillar. When artificial muscles were photopatterned, they wrapped the two pillars on the same side, and the valve core rotated to this side and sealed the corresponding outlet. We prepared the microvalve through multistep polymerization (fig. S4), and the height of the valve core was slightly higher than that of the microchannel, ensuring proper sealing of the valve core without severely impeding its mobility.

For experimental verification, the artificial muscles were photopatterned and drove the valve core from the middle position to outlet 1 within 60 s (Fig. 6B and movie S9). Then, outlet 1 was tightly blocked, as indicated by the blue liquid flowing from the inlet to outlet 2 in Fig. 5B. Then, the molecular motor solution was replenished within 40 s. New artificial muscles were patterned and drove the valve core from outlet 1 to outlet 2 within 120 s (Fig. 6C and movie S10). Thus, outlet 1 was open and outlet 2 was closed, as indicated by the blue liquid flowing from the inlet to outlet 1. These results validate flow switching in the fabricated three-way microvalve, which benefits from the spatial controllability of in situ integration. Compared with common pneumatic valves (*60*), the fabricated valve is easier to fabricate (no control channel) and is actuated internally, rendering it promising for on-site applications and portable devices.

The second example was a gated microcage for trapping micro-objects installed in a 50-μm-thick microchannel with a 200-μm-thick actuation chamber (Fig. 6D). A trapping pocket composed of PDMS posts was fabricated in the center of the structure, as usual for hydrodynamic trapping of micro-objects in microfluidics (*61*, *62*). There was a hydrogel moving gate with a pillar mounted on a rail track for constrained gate motion. Two pairs of PDMS pillars were fixed in the actuation chamber as anchors of the artificial muscle. The hydrogel moving gate functioned as a push-pull sliding door. When the artificial muscles were photopatterned to wrap the pillar of the hydrogel gate and one pair of PDMS pillars, the gate was driven to the upper or lower end of the rail, thus closing or opening the entrance of the trapping pocket. The microcage was prepared through multistep polymerization (fig. S5).

A manipulation experiment using the microcage was conducted using microbeads with diameters of 45 μm. Initially, microbeads dispersed in 1% Triton X-100 solution were introduced into the microchannel, and one was captured by the trapping pocket (Fig. 6E). First, the artificial muscles were photopatterned, and the microcage was closed within 70 s (Fig. 6F and movie S11). When the microcage closed, the microbead was tightly trapped as the flow was reversed. Then, molecular motor solution was replenished within 40 s, and new artificial muscles were reconfigured and opened the microcage within 70 s (Fig. 6G and movie S12). When open, the trapped microbead was released from the microcage as the flow was reversed. This experiment shows that the ability to spatially control the in situ integration enables selective operations, and the temporal controllability enables immediate operations during trapping. This design improves conventional hydrodynamic trapping devices with a new approach to reversibly confine target objects in traps, which may be useful for applications such as isolating objects for time-course analysis and selectively extracting objects for collection or further analysis (*63*, *64*). Compared with the microchamber entrapment approach, in which micro-objects are squeezed through a constriction microchannel to a trapping chamber (*65*, *66*), and the pressure-actuated gate approach (*67*), this microcage needs neither to squeeze objects, thereby avoiding damage, nor a complex control channel.

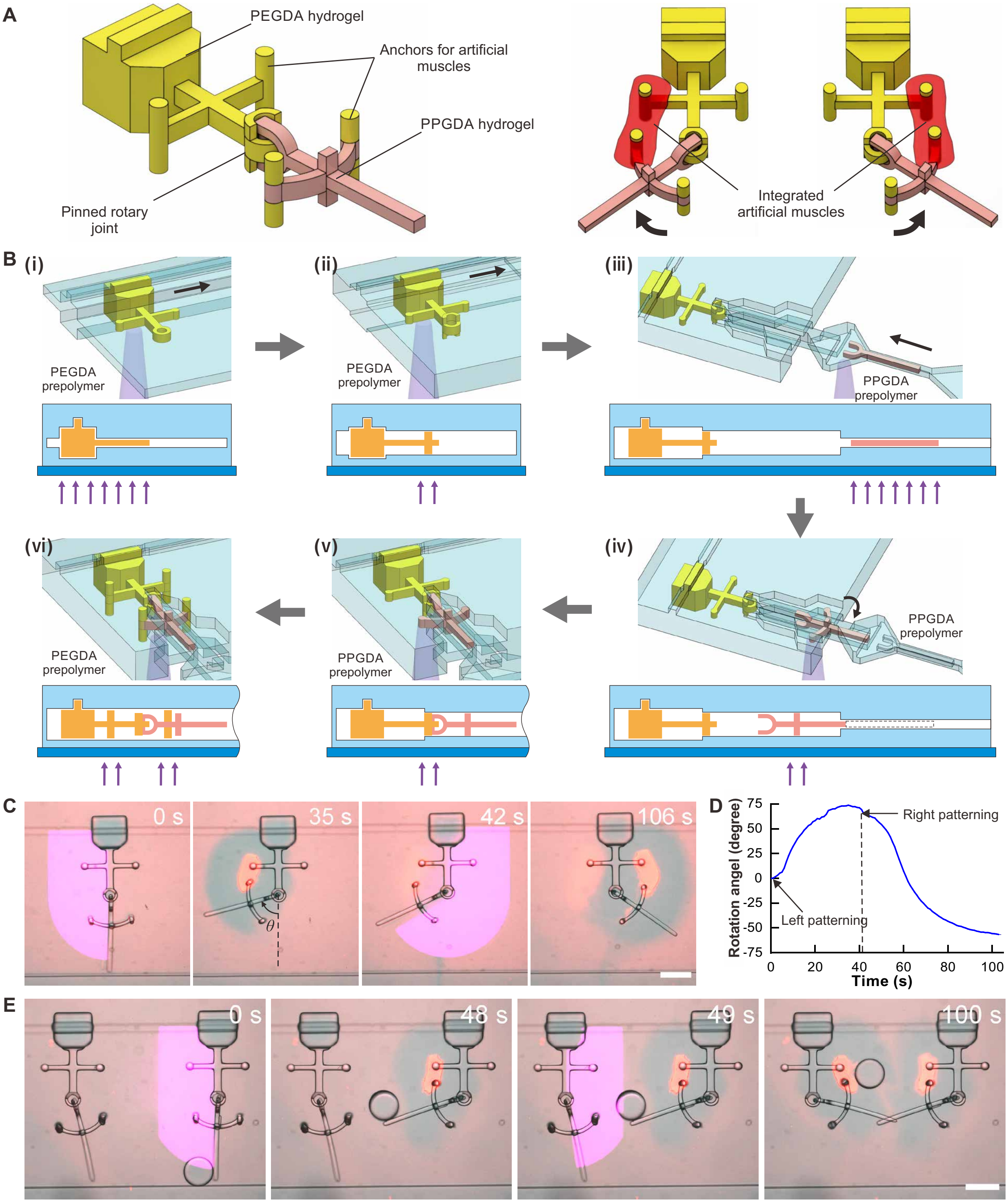

Fig. 5. Microrobot arm demonstrating spatiotemporal controllability of in situ integration. (**A**) Schematic diagrams of the microrobot arm and its bidirectional rotation by selective configuration of artificial muscles. (**B**) Preparation of the microrobot arm (see also movie S5). (**C**) Sequence of microrobot arm actuation when artificial muscles were sequentially patterned on the left and right sides (movie S6). (**D**) Change in rotation angle of joint over time. (**E**) Sequence of grabbing a ball by operating two microrobot arms (movie S8). The artificial muscles were successively configured into the right and left microrobot arms. Scale bars, 200 μm.

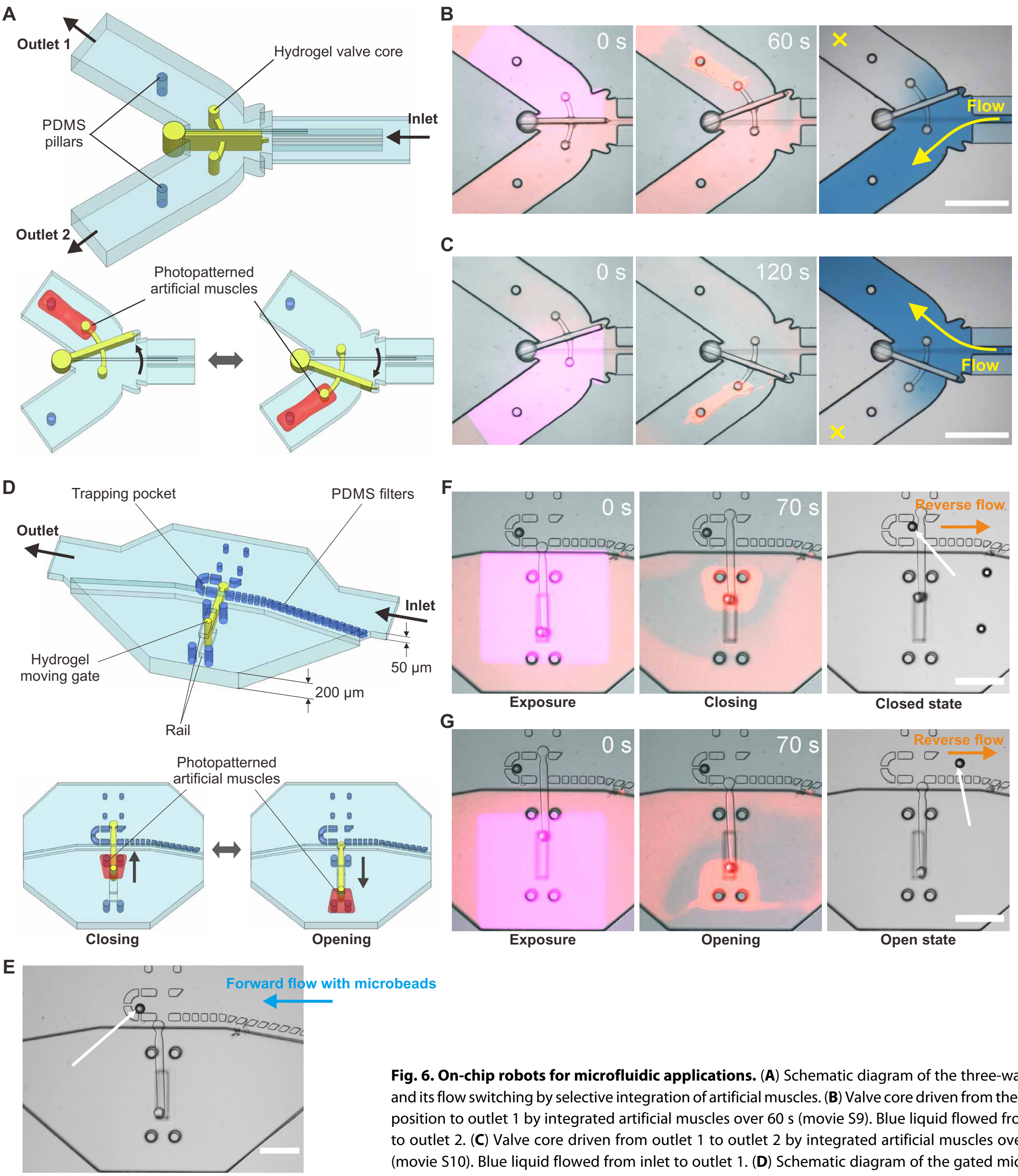

Fig. 6. On-chip robots for microfluidic applications. (**A**) Schematic diagram of the three-way valve and its flow switching by selective integration of artificial muscles. (**B**) Valve core driven from the middle position to outlet 1 by integrated artificial muscles over 60 s (movie S9). Blue liquid flowed from inlet to outlet 2. (**C**) Valve core driven from outlet 1 to outlet 2 by integrated artificial muscles over 120 s (movie S10). Blue liquid flowed from inlet to outlet 1. (**D**) Schematic diagram of the gated microcage and its control (closing and opening) by selective integration of artificial muscles. (**E**) Microbead introduced and captured by the microcage with forward flow. (**F**) Artificial muscles patterned and closed the microcage within 70 s (movie S11). Then, the microbead was tightly trapped in the closed microcage with reverse flow. (**G**) Artificial muscles patterned and opened the microcage within 70 s (movie S12). Then, the trapped microbead was released from the microcage with reverse flow. Scale bars, 500 μm (B and C) and 200 μm (E to G).

DISCUSSION

We propose a microfluidic printing method for microrobot fabrication that integrates artificial muscle actuators in situ, providing spatiotemporal controllability and reconfigurability. The characterized parameters of PEGDA hydrogel helped prepare components with the desired mechanical and geometric properties. In addition, the characterization of the artificial muscles confirmed their appreciable and tunable contractility (0.96 to 1.36 μN) (fig. S11) against the stiffness of PEGDA hydrogel (fig. S10), providing a reference for microrobot design. Different microrobots could potentially be fabricated for various applications using this design (Fig. 2D). One type is to transform the contraction of the artificial muscle into the mechanical deformation of soft hydrogel mechanical structures, such as bending and compression, to perform functions like gripping and pumping. The deformation could be controlled by adjusting structural design through mechanical simulation. Alternatively, rapid springback motions of hydrogel mechanical structures could be realized by incorporating rupture of the artificial muscle into the design of the robot, which might be used for functions based on rapid motion. Another type is to make use of mechanical joints made of multiple hydrogels to perform constrained movements, such as rotation and linear motion with the integration of artificial muscle, which could help construct complex robotic systems and fulfill tasks like object manipulation. Some of these design ideas were brought to fruition through microrobots with different functions in this work.

Microrobot fabrication is largely limited by the manipulation and assembly of microcomponents. Fabrication in multiple sites may not necessarily be compatible with various microrobot applications that require fast fabrication, on-site fabrication, or mass fabrication. To this end, various strategies have been developed, such as fabricating microrobots using composite stimulus-responsive hydrogels as both mechanical components and actuators, thus avoiding assembly (*68*, *69*). As an alternative, we introduce the concept of in situ fabrication and demonstrate the effectiveness of this new paradigm for increasing efficiency, simplifying operation, and improving product consistency as well as providing high adaptability in creating untethered soft robots. Mass production of microrobots has become possible with further improvement in fabrication scalability, and the main challenge now lies in transporting microrobots without damaging the integrated artificial muscle before the next fabrication cycle. This study may make a difference in the development of microrobots and may be useful for applications that have not yet been explored.

This study constituted an application of our printable artificial muscle in practical microrobotics. Its compatibility with printing technologies and microfluidics was demonstrated, and its features of nonreversible contraction and easy disassembly were exploited for reconfigurability, further highlighting its potential for microrobot applications. Although only about eight actuation repetitions through the reconfiguration of artificial muscles were demonstrated here, the cycle can be repeated as many times as the solutions are replenished. On the other hand, some shortcomings of the artificial muscle were revealed, such as its weak contractility and slow strain rate compared with living muscles and other active materials [table S1 (*70*–*74*)]. A limiting factor in its contractility is the rupture of the artificial muscle, because the contractile force reached its maximum immediately before rupture (*36*). Rupture may be prevented by introducing spacer/linker molecules to cross-link microtubules (*75*, *76*) or by adding polyethylene glycol to the buffer to promote depletion-induced microtubule bundling (*77*, *78*).

In this study, microfluidic lithography was used for micromachining and improved by implementing multistep polymerization for 3D-shaped microstructures and multilayered-hydrogel fabrication of movable joints. In addition to the usefulness of these improved strategies for fabricating microrobots in our method, they can also contribute to the development of microfluidic devices. The proposed method led to the development of a type of biohybrid microrobot. In addition to the in situ integration, such microrobots have high biocompatibility, biodegradability, and conversion efficiency and do not require tethering to external energy sources. Moreover, through two-photon lithography, near-infrared light with a large penetration depth of more than 5 mm in biological tissue (*79*) can be used instead of UV light in our method, which makes the in vivo use of such microrobots possible. These features suggest their potential for a wide range of biomedical applications.

MATERIALS AND METHODS

Fabrication of microfluidic chip

Microfluidic chips made of PDMS were fabricated using soft-lithography replica molding. To integrate the artificial muscle with the prepared mechanical structures in the microchannel, there must be enough vertical space between the force-loading part and the microchannel. Therefore, microchannels with a cross-shaped section were necessary for the polymerization of mechanical components with appropriate structures. We used SU-8 multilayer technology (*80*) and automatic alignment and bonding of the PDMS layer (*81*). Figure S6 shows the fabrication process for a representative example. Using photolithography, an SU-8 mold (Nippon Kayaku, Tokyo, Japan) was fabricated on a silicon wafer. A three-layered SU-8 mold was fabricated using triple coating and exposure steps with a single developing step. PDMS (Sylgard 184, Dow Corning, Midland, MI) was poured onto the two molds and baked at 95°C for 1 hour. The demolded PDMS layers were aligned and bonded with methanol lubrication after surface treatment with oxygen plasma. Subsequently, the chip was baked at 90°C for 1 hour to increase the bonding strength.

Experimental setup

An experimental system was set up to help perform tasks in the microfluidic chips (Fig. 1 and fig. S7). The chip was placed on an *xy*-axis stage, and the microrobot fabrication was observed using a microscope (MVX10; Olympus, Tokyo, Japan) with a complementary metal oxide semiconductor camera (GigE Vision XCG-CG510C, Sony, Tokyo, Japan). For bright-field/fluorescence observations, a white light-emitting diode (LED) (MWWHL4, Thorlabs, Newton, NJ) and a 530-nm LED (M530L4, Thorlabs) were used as the light source. All solutions were prefilled in reservoirs (Fluiwell-4C, Fluigent, Le Kremlin-Bicêtre, France) connected to the inlets of the chip. A four-channel pressure controller (MFCS-MZ, Fluigent) and three/two-way valves (2-Switch, Fluigent) were used for solution injection and precise flow control in the microchannels. A high-power LED (CBM-120-UVX, Luminus, Billerica, MA) emitted 365-nm UV light modulated with a digital micromirror device (DLP3010, Texas Instruments, Dallas, TX), and patterned UV irradiation was generated in the microchannels with a 10× objective lens. The control of these devices was integrated into a LabVIEW program.

Preparation of hydrogel prepolymer

PEGDA hydrogel prepolymer solutions were prepared by dissolving 20 to 80% PEGDA [number average molecular weight (Mn) = 700; Sigma-Aldrich, Burlington, MA], 2% photoinitiator, 2-hydroxy-2-methylpropiophenone (Darocur 1173, Sigma-Aldrich), and 0.6% nonionic surfactant (Triton X-100, Sigma-Aldrich) in deionized water.

The PPGDA hydrogel prepolymer solution was prepared by dissolving 60% PPGDA (Mn = 800, Sigma-Aldrich) and 2% photoinitiator, 2-hydroxy-2-methylpropiophenone (Darocur 1173, Sigma-Aldrich) in chloroform.

Preparation of molecular motor solution

Using the same methods presented in our previous work (*36*), CaMLMM and K465m13 were prepared through a series of DNA splicing and expression operations. Tubulin was purified from porcine brain following a tubulin purification protocol (high molarity PIPES buffer) and stained by fluorescent dye (carboxytetramethylrhodamine succinimidyl ester, Sigma-Aldrich). Microtubules were polymerized from fluorescent-labeled tubulin using standard chemical modification (*82*).

Solution A was prepared by mixing 8 μM K465m13 (0.95 mg/ml) and 8 μM CaMLMM (0.91 mg/ml) in a low-salt buffer [20 mM tris-acetate (pH 8.0), 100 mM potassium acetate, 14 mM magnesium sulfate, 10 mM dithiothreitol, 0.01% Triton X-100, 10 mM adenosine triphosphate, and 50 μM paclitaxel]. Solution B was prepared by mixing microtubules (0.78 mg/ml), 10 mM *o*-nitrophenyl EGTA, tetrapotassium salt (NP-EGTA N6802, Invitrogen, Waltham, MA), and 2 mM $CaCl_2$ in the same buffer. The two solutions were mixed equally in the microchannel and introduced into the actuation channel as needed.

Characterization of photopatterned PEGDA hydrogel

To determine the suitable induction conditions for the PEGDA hydrogel and quantitatively control the height of the polymerized structure, we modeled the photopolymerization process based on the simplified reaction-diffusion mechanism (*47*) using the parameters listed in table S2 (*46*, *83*–*85*). The simulation results showed that there was a critical induction time during polymerization, after which the hydrogel height increased almost instantaneously until a critical height was reached, and the height increased gradually afterward. To ensure the achievement of the critical height in the cross-linked hydrogel structure, the induction times for 20, 40, 60, and 80% PEGDA were controlled to 0.30, 0.25, 0.20, and 0.15 s, respectively. For these induction times, the relative thicknesses of oxygen inhibition with different channel heights were calculated and regressed to power functions (fig. S8). Experimental measurements were collected, and the results were consistent with the predictions.

Considering that swelling the polymerized hydrogel structures from the prepolymer solution to the aqueous solution considerably influences the performance of microrobots, we characterized the swelling effect of the PEGDA hydrogel as follows (fig. S9A). Cuboid hydrogels were first polymerized from 20 to 80% PEGDA prepolymer solutions in a 150-μm-thick microchannel and then transferred to deionized water for a 1-hour incubation. By comparing the sizes of the hydrogel cuboids in the relaxed and swollen states, the average elongations in each dimension were calculated as the swelling ratios for different PEGDA concentrations (fig. S9B). Although the swelling of PEGDA hydrogel is affected by the ions in the aqueous solution, this effect is not notable in the case of low concentration (<0.01 M) (*86*). Therefore, these swelling ratios in water were used for approximate calculation in this work.

Stiffness is the most important mechanical property of hydrogels. We used the bending cantilever method to evaluate the Young's modulus of the polymerized PEGDA hydrogels (fig. S10, A and B). A hydrogel cantilever was first fabricated in a 100-μm-thick microchannel and fixed on a platform immersed in deionized water, and its 3D size was measured using a toolmaker's microscope (VHX-D500, Keyence, Osaka, Japan). A microforce sensor (FT-S1000-LAT, FemtoTools, Buchs, Switzerland) was manipulated to bend the cantilever in 0- to 120-μm deflections, and the forces exerted on the tip were recorded. A deflection-force curve was obtained (fig. S10C), and linear regression allowed us to determine the Young's modulus of the hydrogel cantilever according to the simple beam theory (*87*). The results are shown in fig. S10D, where the average Young's modulus increased from 77.5 kPa to 3.82 MPa with increasing PEGDA concentration.

Characterization of photopatterned artificial muscle

In (*36*), we demonstrated the micronewton-level contractility of the developed artificial muscle. To increase the precision of microrobot design, we measured the contractile force of photopatterned artificial muscles exerted on PEGDA hydrogels in PDMS microchannels. The measurement process is illustrated in fig. S11A. A hydrogel structure with two cantilevers was first photopatterned and then transported to a 280-μm-thick microchannel. The artificial muscles were photopatterned in a rectangular area wrapping the tips of the two cantilevers. On the basis of the estimated Young's modulus of the PEGDA hydrogel, we calculated the contractile force applied to the small cantilever by measuring its deflection using a microscope and a motion tracking software (ImageJ). The merged bright-field/fluorescence images in fig. S11B and movie S13 show the contraction of the artificial muscle after 700 μm–by–1400 μm UV irradiation, and fig. S11C shows the corresponding deflection/force-time curve. It took approximately 38 s to reach the maximum force of approximately 1.36 μN.

To evaluate the relation between the contractile force and irradiation area, measurements were acquired for different area widths (L = 1400 μm and W = 300, 500, and 700 μm) and lengths (W = 700 μm and L = 800, 1100, 1400, and 1700 μm), obtaining the results shown in fig. S11 (D and E, respectively). A larger contractile force was achieved when the artificial muscles were activated with a wider irradiation area, and a linear correlation was observed. On the other hand, when the length of the irradiation area was very small, the photopatterned artificial muscles could not anchor the hydrogel cantilevers to generate tensile force. When the irradiation area was long enough to tightly anchor the cantilevers, the force did not change considerably with the length.

Preparation of microwalker

The mechanical structure of the microwalker was polymerized using 60% PEGDA hydrogel in three steps (Fig. 4C). First, a pantograph-shaped body with two fins was polymerized. The body was then transported to a 40-μm-thick microchannel, and two short rear legs were polymerized onto the body. Next, the body was transported to a 240-μm-thick microchannel, and two long front legs were polymerized onto the body. After polymerization, the hydrogel mechanical structure was transported to an actuation channel with a thickness of 310 μm. This process took approximately 3 min.

Preparation of the microrobot arm

The microrobot arm was prepared using the process shown in Fig. 5B (movie S5). First, 60% PEGDA prepolymer was introduced into the microchannel, and the upper arm with a ring was polymerized [Fig. 5B(i)]. The hydrogel was then transported to the second fabrication channel, and a semicircular fence was polymerized onto the ring [Fig. 5B(ii)]. After the upper arm was transported to the third fabrication channel, the PPGDA prepolymer was introduced into the channel, and a Y-shaped forearm was polymerized [Fig. 5B(iii)]. The forearm turned around when it was hydrodynamically pushed into a vertical channel. The PPGDA extension was polymerized onto the forearm [Fig. 5B(iv)]. Next, the forearm was transported to the upper arm and stopped by a fence on the ring. A pillar was polymerized in the ring as the joint pin that connected the upper arm and forearm and allowed relative rotation about a single axis [Fig. 5B(iii)]. Last, the PEGDA prepolymer was reinjected into the channel, and four pillars were polymerized [Fig. 5B(vi)]. After fabrication, the microrobot arm was transported to the actuation channel. This process took about 8 min.

Preparation of the three-way microvalve

The three-way microvalve was prepared in three steps (fig. S4). First, 40% PEGDA hydrogel prepolymer was introduced into the fabrication channel. The main structure of the valve core was polymerized in the inlet with a cross-shaped section. Then, the polymerized structure was rail-guided into the Y-shaped joint, and pillars were polymerized on both sides of the valve core. Last, one end of the valve core was moved into a circular slot, and a cylindrical hydrogel structure was polymerized in situ. After polymerization, a 0.5% Triton X-100 solution was introduced into the channel to remove the remaining prepolymer. This process took about 4 min.

According to the characterized swelling ratio of the PEGDA hydrogel and the thickness of the oxygen inhibition layer, the swelled hydrogel valve core had a height of 205 μm, slightly higher than the microchannel (height of 200 μm) to ensure proper sealing of the valve core without severely impeding its mobility.

Preparation of the gated microcage

The gated microcage was prepared in two steps (fig. S5). A 40% PEGDA hydrogel prepolymer solution was introduced into the microchannel, and the main body of the moving gate was polymerized in a 50-μm-thick area. Then, the polymerized hydrogel structure was moved to the actuation chamber until it reached the rail. A pillar was polymerized in situ at the end of the moving gate in the rail track. This process took about 3 min.

SUPPLEMENTARY MATERIALS

www.science.org/doi/10.1126/scirobotics.aba8212
Figs. S1 to S11
Tables S1 and S2
Movies S1 to S13
MDAR Reproducibility Checklist

REFERENCES AND NOTES

1. S. Zhang, E. Y. Scott, J. Singh, Y. Chen, Y. Zhang, M. Elsayed, M. D. Chamberlain, N. Shakiba, K. Adams, S. Yu, C. M. Morshead, P. W. Zandstra, A. R. Wheeler, The optoelectronic microrobot: A versatile toolbox for micromanipulation. *Proc. Natl. Acad. Sci.* **116**, 14823–14828 (2019).
2. M. Hagiwara, T. Kawahara, Y. Yamanishi, T. Masuda, L. Feng, F. Arai, On-chip magnetically actuated robot with ultrasonic vibration for single cell manipulations. *Lab Chip* **11**, 2049–2054 (2011).
3. X. Dong, S. Kheiri, Y. Lu, Z. Xu, M. Zhen, X. Liu, Toward a living soft microrobot through optogenetic locomotion control of *Caenorhabditis elegans*. *Sci. Robot.* **6**, eabe3950 (2021).
4. S. Zhang, M. Elsayed, R. Peng, Y. Chen, Y. Zhang, J. Peng, W. Li, M. D. Chamberlain, A. Nikitina, S. Yu, X. Liu, S. L. Neale, A. R. Wheeler, Reconfigurable multi-component micromachines driven by optoelectronic tweezers. *Nat. Commun.* **12**, 5349 (2021).
5. J. Li, B. Esteban-Fernández de Ávila, W. Gao, L. Zhang, J. Wang, Micro/nanorobots for biomedicine: Delivery, surgery, sensing, and detoxification. *Sci. Robot.* **2**, eaam6431 (2017).
6. C. Hu, S. Pané, B. J. Nelson, Soft micro- and nanorobotics. *Annu. Rev. Control Robot. Autonom. Syst.* **1**, 53–75 (2018).
7. S. I. Rich, R. J. Wood, C. Majidi, Untethered soft robotics. *Nat. Electron.* **1**, 102–112 (2018).
8. H. Kim, S. K. Ahn, D. M. Mackie, J. Kwon, S. H. Kim, C. Choi, Y. H. Moon, H. B. Lee, S. H. Ko, Shape morphing smart 3D actuator materials for micro soft robot. *Mater. Today* **41**, 243–269 (2020).
9. M. Z. Miskin, A. J. Cortese, K. Dorsey, E. P. Esposito, M. F. Reynolds, Q. Liu, M. Cao, D. A. Muller, P. L. McEuen, I. Cohen, Electronically integrated, mass-manufactured, microscopic robots. *Nature* **584**, 557–561 (2020).
10. M. Garcés-Schröder, L. Hecht, A. Vierheller, M. Leester-Schädel, M. Böl, A. Dietzel, Micro-grippers with femtosecond-laser machined in-plane agonist-antagonist SMA actuators integrated on wafer-level by galvanic riveting. *Proceedings* **1**, 385 (2017).
11. J. Li, M. Pumera, 3D printing of functional microrobots. *Chem. Soc. Rev.* **50**, 2794–2838 (2021).
12. M. Dong, X. Wang, X. Z. Chen, F. Mushtaq, S. Deng, C. Zhu, H. Torlakcik, A. Terzopoulou, X. H. Qin, X. Xiao, J. Puigmartí-Luis, H. Choi, A. P. Pêgo, Q. D. Shen, B. J. Nelson, S. Pané, 3D-printed soft magnetoelectric microswimmers for delivery and differentiation of neuron-like cells. *Adv. Funct. Mater.* **30**, 1910323 (2020).
13. X. Ji, X. Liu, V. Cacucciolo, M. Imboden, Y. Civet, A. E. Haitami, S. Cantin, Y. Perriard, H. Shea, An autonomous untethered fast soft robotic insect driven by low-voltage dielectric elastomer actuators. *Sci. Robot.* **4**, eaaz6451 (2019).
14. X. Yang, L. Chang, N. O. Pérez-Arancibia, An 88-milligram insect-scale autonomous crawling robot driven by a catalytic artificial muscle. *Sci. Robot.* **5**, eaba0015 (2020).
15. C. Ahn, X. Liang, S. Cai, Bioinspired design of light-powered crawling, squeezing, and jumping untethered soft robot. *Adv. Mater. Technol.* **4**, 1900185 (2019).
16. Y. Tanaka, K. Morishima, T. Shimizu, A. Kikuchi, M. Yamato, T. Okano, T. Kitamori, An actuated pump on-chip powered by cultured cardiomyocytes. *Lab Chip* **6**, 362–368 (2006).
17. Y. Akiyama, K. Iwabuchi, Y. Furukawa, K. Morishima, Long-term and room temperature operable bioactuator powered by insect dorsal vessel tissue. *Lab Chip* **9**, 140–144 (2009).
18. L. Sun, Y. Yu, Z. Chen, F. Bian, F. Ye, L. Sun, Y. Zhao, Biohybrid robotics with living cell actuation. *Chem. Soc. Rev.* **49**, 4043–4069 (2020).
19. Y. Chen, H. Wang, E. F. Helbling, N. T. Jafferis, R. Zufferey, A. Ong, K. Ma, N. Gravish, P. Chirarattananon, M. Kovac, R. J. Wood, A biologically inspired, flapping-wing, hybrid aerial-aquatic microrobot. *Sci. Robot.* **2**, (2017).
20. R. Bogue, Assembly of 3D micro-components: A review of recent research. *Assembly Autom.* **31**, 309–314 (2011).
21. C. J. Morris, S. A. Stauth, B. A. Parviz, Self-assembly for microscale and nanoscale packaging: Steps toward self-packaging. *IEEE Trans. Adv. Packaging* **28**, 600–611 (2005).
22. D. Li, Y. Liu, Y. Yang, Y. Shen, A fast and powerful swimming microrobot with a serrated tail enhanced propulsion interface. *Nanoscale* **10**, 19673–19677 (2018).
23. Y. Morimoto, H. Onoe, S. Takeuchi, Biohybrid robot powered by an antagonistic pair of skeletal muscle tissues. *Sci. Robot.* **3**, eaat4440 (2018).
24. V. Chan, K. Park, M. B. Collens, H. Kong, T. A. Saif, R. Bashir, Development of miniaturized walking biological machines. *Sci. Rep.* **2**, 857 (2012).
25. J. Hill, R. Wildman, A. Mata, Exploiting the fundamentals of biological organization for the advancement of biofabrication. *Curr. Opin. Biotechnol.* **74**, 42–54 (2022).
26. A. H. Huang, Coordinated development of the limb musculoskeletal system: Tendon and muscle patterning and integration with the skeleton. *Dev. Biol.* **429**, 420–428 (2017).
27. M. Wehner, R. L. Truby, D. J. Fitzgerald, B. Mosadegh, G. M. Whitesides, J. A. Lewis, R. J. Wood, An integrated design and fabrication strategy for entirely soft, autonomous robots. *Nature* **536**, 451–455 (2016).
28. T. J. Jones, E. Jambon-Puillet, J. Marthelot, P.-T. Brun, Bubble casting soft robotics. *Nature* **599**, 229–233 (2021).
29. R. D. Vale, R. A. Milligan, The way things move: Looking under the hood of molecular motor proteins. *Science* **288**, 88–95 (2000).
30. T. Torisawa, D. Taniguchi, S. Ishihara, K. Oiwa, Spontaneous formation of a globally connected contractile network in a microtubule-motor system. *Biophys. J.* **111**, 373–385 (2016).
31. G. H. Koenderink, E. K. Paluch, Architecture shapes contractility in actomyosin networks. *Curr. Opin. Cell Biol.* **50**, 79–85 (2018).
32. D. Needleman, Z. Dogic, Active matter at the interface between materials science and cell biology. *Nat. Rev. Mater.* **2**, 17048 (2017).
33. O. Lieleg, M. M. Claessens, A. R. Bausch, Structure and dynamics of cross-linked actin networks. *Soft Matter* **6**, 218–225 (2010).
34. K. Matsuda, A. M. R. Kabir, N. Akamatsu, A. Saito, S. Ishikawa, T. Matsuyama, O. Ditzer, M. S. Islam, Y. Ohya, K. Sada, A. Konagaya, A. Kuzuya, A. Kakugo, Artificial smooth muscle model composed of hierarchically ordered microtubule asters mediated by DNA origami nanostructures. *Nano Lett.* **19**, 3933–3938 (2019).
35. Y. Vyborna, J.-C. Galas, A. Estevez-Torres, DNA-controlled spatiotemporal patterning of a cytoskeletal active gel. *J. Am. Chem. Soc.* **143**, 20022–20026 (2021).
36. T. Nitta, Y. Wang, Z. Du, K. Morishima, Y. Hiratsuka, A printable active network actuator built from an engineered biomolecular motor. *Nat. Mater.* **20**, 1149–1155 (2021).
37. H. Hess, Muscle on demand. *Nat. Mater.* **20**, 1040–1041 (2021).

38. D. J. Beebe, J. S. Moore, J. M. Bauer, Q. Yu, R. H. Liu, C. Devadoss, B. H. Jo, Functional hydrogel structures for autonomous flow control inside microfluidic channels. *Nature* **404**, 588–590 (2000).
39. D. Dendukuri, D. C. Pregibon, J. Collins, T. A. Hatton, P. S. Doyle, Continuous-flow lithography for high-throughput microparticle synthesis. *Nat. Mater.* **5**, 365–369 (2006).
40. S. E. Chung, W. Park, S. Shin, S. A. Lee, S. Kwon, Guided and fluidic self-assembly of microstructures using railed microfluidic channels. *Nat. Mater.* **7**, 581–587 (2008).
41. A. Richter, S. Klatt, G. Paschew, C. Klenke, Micropumps operated by swelling and shrinking of temperature-sensitive hydrogels. *Lab Chip* **9**, 613–618 (2009).
42. Q. T. Nguyen, Y. Hwang, A. C. Chen, S. Varghese, R. L. Sah, Cartilage-like mechanical properties of poly(ethylene glycol)-diacrylate hydrogels. *Biomaterials* **33**, 6682–6690 (2012).
43. J.-Y. Sun, X. Zhao, W. R. K. Illeperuma, O. Chaudhuri, K. H. Oh, D. J. Mooney, J. J. Vlassak, Z. Suo, Highly stretchable and tough hydrogels. *Nature* **489**, 133–136 (2012).
44. M. Nagai, K. Kato, T. Shibata, Underwater motion of hydrogel microstructure by optofluidic lithography studied with gap control and object holding platform. *Microelectron. Eng.* **164**, 108–114 (2016).
45. Y. Wang, K. Toyoda, K. Uesugi, K. Morishima, A simple micro check valve using a photo-patterned hydrogel valve core. *Sens. Actuat. A Phys.* **304**, 111878 (2020).
46. C. Decker, A. D. Jenkins, Kinetic approach of oxygen inhibition in ultraviolet- and laser-induced polymerizations. *Macromolecules* **18**, 1241–1244 (1985).
47. D. Dendukuri, P. Panda, R. Haghgooie, J. M. Kim, T. A. Hatton, P. S. Doyle, Modeling of oxygen-inhibited free radical photopolymerization in a PDMS microfluidic device. *Macromolecules* **41**, 8547–8556 (2008).
48. W. Park, H. Lee, H. Park, S. Kwon, Sorting directionally oriented microstructures using railed microfluidics. *Lab Chip* **9**, 2169–2175 (2009).
49. L. J. Millet, E. A. Corbin, R. Free, K. Park, H. Kong, W. P. King, R. Bashir, Characterization of mass and swelling of hydrogel microstructures using MEMS resonant mass sensor arrays. *Small* **8**, 2555–2562 (2012).
50. D. L. Taylor, M. Panhuis, Self-healing hydrogels. *Adv. Mater.* **28**, 9060–9093 (2016).
51. Z. Wei, J. He, T. Liang, H. Oh, J. Athas, Z. Tong, C. Wang, Z. Nie, Autonomous self-healing of poly (acrylic acid) hydrogels induced by the migration of ferric ions. *Polym. Chem.* **4**, 4601–4605 (2013).
52. J. A. Martinez, R. R. Panepucci, Design, fabrication, and characterization of a microgripper device, in *Proceedings of the Florida Conference on Recent Advances in Robotics* (University of South Florida, 2007).
53. F. Beyeler, A. Neild, S. Oberti, D. J. Bell, Y. Sun, J. Dual, B. J. Nelson, Monolithically fabricated microgripper with integrated force sensor for manipulating microobjects and biological cells aligned in an ultrasonic field. *J. Microelectromech. Syst.* **16**, 7–15 (2007).
54. K.-i. Kabumoto, T. Hoshino, Y. Akiyama, K. Morishima, Voluntary movement controlled by the surface EMG signal for tissue-engineered skeletal muscle on a gripping tool. *Tissue Eng. Part A* **19**, 1695–1703 (2013).
55. M. Sitti, *Mobile Microrobotics* (MIT Press, 2017).
56. Y. Akiyama, K. Odaira, K. Sakiyama, T. Hoshino, K. Iwabuchi, K. Morishima, Rapidly-moving insect muscle-powered microrobot and its chemical acceleration. *Biomed. Microdevices* **14**, 979–986 (2012).
57. L. Ricotti, B. Trimmer, A. W. Feinberg, R. Raman, K. K. Parker, R. Bashir, M. Sitti, S. Martel, P. Dario, A. Menciassi, Biohybrid actuators for robotics: A review of devices actuated by living cells. *Sci. Robot.* **2**, eaaq0495 (2017).
58. Y.-Y. Lin, E. R. Welch, R. B. Fair, Low voltage picoliter droplet manipulation utilizing electrowetting-on-dielectric platforms. *Sens. Actuators B* **173**, 338–345 (2012).
59. J. Shin, H. Park, C.-W. Kim, S.-J. Kim, Elastomeric microfluidic valve with low, constant opening threshold pressure. *RSC Adv.* **5**, 23239–23245 (2015).
60. A. K. Au, H. Lai, B. R. Utela, A. Folch, Microvalves and micropumps for BioMEMS. *Micromachines* **2**, 179–220 (2011).
61. M. Tanyeri, C. Schroeder, Flow-based particle trapping and manipulation, in *Encyclopedia of Microfluidics and Nanofluidics* (Springer, 2014), pp. 1–9.
62. V. Narayanamurthy, S. Nagarajan, F. Samsuri, T. Sridhar, Microfluidic hydrodynamic trapping for single cell analysis: Mechanisms, methods and applications. *Anal. Methods* **9**, 3751–3772 (2017).
63. J. Nilsson, M. Evander, B. Hammarström, T. Laurell, Review of cell and particle trapping in microfluidic systems. *Anal. Chim. Acta* **649**, 141–157 (2009).
64. Q. Luan, C. Macaraniag, J. Zhou, I. Papautsky, Microfluidic systems for hydrodynamic trapping of cells and clusters. *Biomicrofluidics* **14**, 031502 (2020).
65. X. Ren, B. M. Foster, P. Ghassemi, J. S. Strobl, B. A. Kerr, M. Agah, Entrapment of prostate cancer circulating tumor cells with a sequential size-based microfluidic chip. *Anal. Chem.* **90**, 7526–7534 (2018).
66. S. S. Bithi, S. A. Vanapalli, Microfluidic cell isolation technology for drug testing of single tumor cells and their clusters. *Sci. Rep.* **7**, 41707 (2017).
67. H. S. Kim, T. P. Devarenne, A. Han, A high-throughput microfluidic single-cell screening platform capable of selective cell extraction. *Lab Chip* **15**, 2467–2475 (2015).
68. J. Yunas, B. Mulyanti, I. Hamidah, M. Mohd Said, R. E. Pawinanto, W. A. F. Wan Ali, A. Subandi, A. A. Hamzah, R. Latif, B. Yeop Majlis, Polymer-based MEMS electromagnetic actuator for biomedical application: A review. *Polymers* **12**, 1184 (2020).
69. H. Banerjee, M. Suhail, H. Ren, Hydrogel actuators and sensors for biomedical soft robots: Brief overview with impending challenges. *Biomimetics* **3**, 15 (2018).
70. R. M. Duffy, A. W. Feinberg, Engineered skeletal muscle tissue for soft robotics: Fabrication strategies, current applications, and future challenges. *Wiley Interdiscip. Rev. Nanomed. Nanobiotechnol.* **6**, 178–195 (2014).
71. T. Tanimoto, K. Okazaki, K. Yamamoto, Tensile stress-strain behavior of piezoelectric ceramics. *Jpn. J. Appl. Phys.* **32**, 4233–4236 (1993).
72. I. Hunter, S. Lafontaine, J. Hollerbach, P. Hunter, Fast reversible NiTi fibers for use in microrobotics, in *Proceedings of the 1991 IEEE Micro Electro Mechanical Systems-MEMS* (IEEE, 1991), vol. 91, pp. 166–170.
73. Q. Zhang, V. Bharti, X. Zhao, Giant electrostriction and relaxor ferroelectric behavior in electron-irradiated poly (vinylidene fluoride-trifluoroethylene) copolymer. *Science* **280**, 2101–2104 (1998).
74. I. W. Hunter, S. Lafontaine, in *Technical Digest IEEE Solid-State Sensor and Actuator Workshop* (IEEE, 1992), pp. 178–185.
75. R. Subramanian, E. M. Wilson-Kubalek, C. P. Arthur, M. J. Bick, E. A. Campbell, S. A. Darst, R. A. Milligan, T. M. Kapoor, Insights into antiparallel microtubule crosslinking by PRC1, a conserved nonmotor microtubule binding protein. *Cell* **142**, 433–443 (2010).
76. S. N. Ricketts, M. L. Francis, L. Farhadi, M. J. Rust, M. Das, J. L. Ross, R. M. Robertson-Anderson, Varying crosslinking motifs drive the mesoscale mechanics of actin-microtubule composites. *Sci. Rep.* **9**, 12831 (2019).
77. T. Sanchez, Z. Dogic, Engineering oscillating microtubule bundles. *Methods Enzymol.* **524**, 205–224 (2013).
78. V. Nasirimarekani, T. Strübing, A. Vilfan, I. Guido, Tuning the properties of active microtubule networks by depletion forces. *Langmuir* **37**, 7919–7927 (2021).
79. C. Ash, M. Dubec, K. Donne, T. Bashford, Effect of wavelength and beam width on penetration in light-tissue interaction using computational methods. *Lasers Med. Sci.* **32**, 1909–1918 (2017).
80. A. Mata, A. J. Fleischman, S. Roy, Fabrication of multi-layer SU-8 microstructures. *J. Micromech. Microeng.* **16**, 276–284 (2006).
81. J. Y. Kim, J. Y. Baek, K. A. Lee, S. H. Lee, Automatic aligning and bonding system of PDMS layer for the fabrication of 3D microfluidic channels. *Sens Actuat. A Phys.* **119**, 593–598 (2005).
82. A. Hyman, D. Drechsel, D. Kellogg, S. Salser, K. Sawin, P. Steffen, L. Wordeman, T. Mitchison, Preparation of modified tubulins, in *Methods in Enzymology* (Elsevier, 1991), vol. 196, pp. 478–485.
83. S. Kızılel, V. H. Pérez-Luna, F. Teymour, Mathematical model for surface-initiated photopolymerization of poly (ethylene glycol) diacrylate. *Macromol. Theory Simulations* **15**, 686–700 (2006).
84. D. Debroy, J. Oakey, D. Li, Interfacially-mediated oxygen inhibition for precise and continuous poly (ethylene glycol) diacrylate (PEGDA) particle fabrication. *J. Colloid Interface Sci.* **510**, 334–344 (2018).
85. L. Lecamp, P. Lebaudy, B. Youssef, C. Bunel, Influence of UV radiation wavelength on conversion and temperature distribution profiles within dimethacrylate thick material during photopolymerization. *Polymer* **42**, 8541–8547 (2001).
86. K. Nalampang, R. Panjakha, R. Molloy, B. J. Tighe, Structural effects in photopolymerized sodium AMPS hydrogels crosslinked with poly (ethylene glycol) diacrylate for use as burn dressings. *J. Biomater. Sci. Polym. Ed.* **24**, 1291–1304 (2013).
87. F. Beer, *Mechanics of Materials* (McGraw-Hill, 2019).

Acknowledgments: We thank Z. Du, K. Minakata, and K. Uesugi for technical support in the preparation of the molecular motors and the construction of the systems used in this study. **Funding:** This work was supported by the New Energy and Industrial Technology Development Organization (NEDO), the Japan Society for the Promotion of Science Grants-in-Aid for Scientific Research (KAKENHI) (grant nos. 19H02106, 21 K18700, 21H05880, 22H00196, and 22H04951), and the China Scholarship Council (CSC) (to Y.W., grant no. 201606320248). **Author contributions:** Conceptualization: Y.H. and K.M. Methodology: Y.W., T.N., Y.H., and K.M. Investigation: Y.W. and K.M. Visualization: Y.W. and K.M. Funding acquisition: T.N., Y.H., and K.M. Project administration: K.M. Writing—original draft: Y.W. and K.M. Writing—review and editing: Y.W., T.N., Y.H., and K.M. **Competing interests:** The authors declare that they have no competing interests. **Data and materials availability:** All data are presented in the paper and in the Supplementary Materials. Additional information can be provided by K.M. upon reasonable request.

Submitted 17 December 2021
Accepted 27 July 2022
Published 24 August 2022
10.1126/scirobotics.aba8212

Science Robotics

In situ integrated microrobots driven by artificial muscles built from biomolecular motors

Yingzhe Wang, Takahiro Nitta, Yuichi Hiratsuka, and Keisuke Morishima

Sci. Robot. **7** (69), eaba8212. DOI: 10.1126/scirobotics.aba8212

Science Robotics (ISSN 2470-9476) is published by the American Association for the Advancement of Science. 1200 New York Avenue NW, Washington, DC 20005. The title *Science Robotics* is a registered trademark of AAAS.